



Article

The Approximate Analytical Solution for the Top-of-Atmosphere Spectral Reflectance of Atmosphere—Underlying Snow System over Antarctica

Alexander Kokhanovsky

Max Planck Institute for Chemistry, Hahn-Meitner-Weg 1, 55128 Mainz, Germany; a.a.kokhanovsky@gmail.com

Abstract: The analytical solutions of the radiative transfer equation are needed for the solution of various applied atmospheric and snow optics problems. In this paper, we propose a simple analytical equation for the top-of-atmosphere (TOA) spectral reflectance. To simplify the problem under study we consider the case of Antarctica, where both snow and atmosphere are almost free of pollutants. This work is focused on the simulation of the moderate spectral resolution TOA measurements (1 nm or so) and the spectral range 400–1000 nm. The values of the coefficient of variance (CV) between the measured by the Ocean and Land Colour Instrument (OLCI) on board Sentinel-3A and modelled spectra are smaller than 10% for most cases in Antarctica. There are regions in Eastern Antarctica, where the values of CV are smaller than 5%. The areas with larger deviations between measured and retrieved spectra could be due to the presence of clouds or structures on the snow surface not captured by the proposed model.

Keywords: radiative transfer; snow; aerosol; atmosphere; molecular scattering; ozone; water vapor; oxygen



Citation: Kokhanovsky, A. The Approximate Analytical Solution for the Top-of-Atmosphere Spectral Reflectance of Atmosphere—Underlying Snow System over Antarctica. *Remote Sens.* **2022**, *14*, 4778. <https://doi.org/10.3390/rs14194778>

Academic Editor: Jie Cheng

Received: 12 August 2022

Accepted: 19 September 2022

Published: 24 September 2022

Publisher's Note: MDPI stays neutral with regard to jurisdictional claims in published maps and institutional affiliations.



Copyright: © 2022 by the author. Licensee MDPI, Basel, Switzerland. This article is an open access article distributed under the terms and conditions of the Creative Commons Attribution (CC BY) license (<https://creativecommons.org/licenses/by/4.0/>).

1. Introduction

The optical signals detected on multiple satellite platforms over snow surfaces are determined by the optical properties of the snow surface and atmosphere. The solution of both direct and inverse problems of an atmosphere—underlying snow system requires simple relationships between top-of-atmosphere (TOA) reflectance R and the microphysical/optical characteristics of both snow and atmosphere. The task of this paper is to present a simple analytical relationship between the value of R as detected on a satellite with atmosphere/snow properties. Such a relationship can be established using a numerical solution of an integro-differential radiative transfer equation (RTE) [1]. However, this path is quite complicated and time-consuming. The analytical solutions of RTE are needed for the solution of various applied atmospheric and snow optics problems [2–5]. This is the main driver of this work. To simplify the problem under study we consider the case of Antarctica, where both snow and atmosphere are almost free of pollutants. This work is focused on the simulation of the moderate spectral resolution TOA measurements (1 nm or so) and the spectral range 400–1000 nm.

In the next section, we present the TOA reflectance model. Section 3 is devoted to the application of the model to the measurements performed by the Ocean and Land Colour Instrument (OLCI) on board Sentinel-3.

2. The Top-of-Atmosphere Reflectance Model

2.1. The Reflection of Light from Atmosphere—Underlying Surface System

The top-of atmosphere spectral reflectance over a Lambertian surface with albedo r_s can be presented in the following way [1,6]:

$$R = \left(R_a + \frac{T_a r_s}{1 - r_a r_s} \right) T_g \tag{1}$$

Here, the values of R_a , r_a , and T_a represent the reflectance, albedo, and total transmittance, respectively, for the artificial atmosphere without gaseous absorbers and black underlying surface, T_g is the gaseous transmittance. The snow is close to the Lambertian surface in the visible. However, there are differences. Therefore, to account for the non-Lambertian effects we substitute the snow albedo in the nominator of Equation (1) by the snow spectral reflectance R_s . Then it follows [7]:

$$R = (R_a + \gamma T_a R_s) T_g \tag{2}$$

where $\gamma = (1 - r_a r_s)^{-1}$. It follows from Equation (2) that $R \rightarrow R_s$ at atmospheric optical thickness $\tau \rightarrow 0$ outside gaseous absorption bands as it should be. This is because $R_a \rightarrow 0$, $r_a \rightarrow 0$ and $T_a \rightarrow 1$, $T_g = 1$ in this case by the definition. The errors of Equation (2) increase with the deviation of the underlying surface from the Lambertian one and also with the increase in optical thickness τ . Then, yet another approach for the account of underlying surface effects on the value of TOA reflectance must be used (see, e.g., [8]).

However, the focus of this paper is the simulation of satellite optical signals over Antarctica, where τ is small and the error of this approximation is acceptable for the solution of most practical problems related, e.g., to snow remote sensing from space [7].

One can see that the desired analytical solution to the problem at hand can be obtained if analytical equations for all functions in Equation (2) are known. The analytical solutions for the corresponding functions are considered in the next section.

2.2. The Atmospheric Path Reflectance

The atmospheric path reflectance R_a can be presented in the following way using the Sobolev approximation [7,9,10]:

$$R_a = R_{ss} + R_{ms} \tag{3}$$

where the single scattering contribution can be presented as

$$R_{ss} = M(\tau)p(\theta), \tag{4}$$

$$M(\tau) = \frac{1 - \exp(-m\tau)}{4(\mu_0 + \mu)}, \tag{5}$$

$$m = \mu_0^{-1} + \mu^{-1}. \tag{6}$$

Here, μ_0 is the cosine of the solar zenith angle (SZA), μ is the cosine of the viewing zenith angle (VZA), θ is the scattering angle defined as

$$\cos \theta = -\mu_0 \mu + s_0 s \cos \varphi, \tag{7}$$

φ is the relative azimuthal angle (RAA), s_0 is the sine of the SZA, s is the sine of the VZA, τ is the atmospheric optical thickness, $p(\theta)$ is the phase function.

The multiple light scattering contribution R_{ms} can be approximated as [9]:

$$R_{ms} = 1 + M(\tau)q(\mu_0, \mu) - \frac{N(\tau)}{1 + 0.75(1 - g)\tau} \tag{8}$$

where

$$N(\tau) = f(\mu_0)f(\mu), \quad (9)$$

$$f(\mu_0) = \frac{1}{2} \left\{ 1 + \frac{3}{2}\mu_0 + \left(1 - \frac{3}{2}\mu_0 \right) \exp\left(-\frac{\tau}{\mu_0}\right) \right\}, \quad (10)$$

$$q(\mu_0, \mu) = 3(1 + g)\mu_0\mu - 2(\mu_0 + \mu). \quad (11)$$

The value of the average cosine of scattering angle g is determined by the following expression:

$$g = \frac{1}{2} \int_0^\pi p(\theta) \sin\theta \cos\theta \, d\theta. \quad (12)$$

Equation (8) can be substituted by other approximations or parameterisations [3,11] if needed.

Equations (3), (4) and (8) make it possible to calculate the path reflectance analytically for a given phase function $p(\theta)$ and atmospheric optical thickness τ . The approximate account for aerosol absorption effects can be performed multiplying R_{ss} by the single scattering albedo ω_0 . It follows from Equation (8) that $R_{ms} \rightarrow 0$ as $\tau \rightarrow 0$ as it should be. The accuracy of the Sobolev approximation has been thoroughly studied [10,12,13]. It has been found that the error of this approximation is smaller than 10% for most of the observation geometries at SZA and VZA smaller than 75 degrees, and an atmospheric optical thickness smaller than 0.5, which is the case for an atmospheric layer above Antarctica.

The accuracy of the Sobolev approximation presented here increases as $g \rightarrow 0$, which is the case for the clean atmosphere of Antarctica. Indeed, the atmospheric optical thickness outside gaseous absorption bands can be presented as

$$\tau(\lambda) = \tau_{mol}(\lambda) + \tau_{aer}(\lambda), \quad (13)$$

where λ is the wavelength, τ_{mol} is the molecular optical thickness, τ_{aer} is the aerosol optical thickness (AOT). Let us take the wavelength of 400 nm. In this case, one can assume that $\tau_{mol} = 0.23$ [14] and $\tau_{aer} = 0.02$ [15] at Dome C in Antarctica. One can see that atmospheric molecular scattering and extinction processes are far more important at 400 nm as compared to light scattering by atmospheric aerosol.

The atmospheric phase function for a vertically homogeneous nonabsorbing atmospheric layer can be presented as:

$$p(\theta) = \frac{\tau_{mol}p_{mol}(\theta) + \tau_{aer}p_{aer}(\theta)}{\tau_{mol} + \tau_{aer}}, \quad (14)$$

where

$$p_{mol}(\theta) = \frac{3}{4} (1 + \cos^2\theta) \quad (15)$$

is the molecular scattering phase function and $p_{aer}(\theta)$ is the aerosol phase function. It follows from Equations (12) and (14):

$$g = \frac{\tau_{aer}g_{aer}}{\tau_{mol} + \tau_{aer}}, \quad (16)$$

where g_{aer} is the average cosine of scattering angle for atmospheric aerosol. Taking into account that $g_{aer} \approx 0.7$ at 400 nm [7], we have the following estimation: $g \approx 0.06$ at Dome C and the proposed approximation for R_{ms} can be used with high accuracy at 400 nm at elevated sites in Antarctica. The value of g somewhat increases at coastal sites being smaller than 0.1–0.2 at 400 nm in most cases. At longer wavelengths, the contribution of multiple scattering decreases and $R_a \rightarrow R_{ss}$. Therefore, the errors in the approximation for the value of R_{ms} become irrelevant. This explains the applicability of the Sobolev approximation derived at small values of g for the studied case of the Antarctic atmosphere. The

approximation can be further improved using the truncation approximation as discussed in [10], where also the accuracy of the Sobolev approximation is studied.

We use the following approximation for the spectral aerosol optical thickness [16]:

$$\tau_{aer}(\lambda) = \tau_{aer}(\lambda_0) \left(\frac{\lambda}{\lambda_0} \right)^{-\alpha}, \quad (17)$$

where $\lambda_0 = 1 \mu\text{m}$, and the pair α and $\beta = \tau_{aer}(\lambda_0)$ represent the Angström parameters. The molecular optical thickness is represented as [17]

$$\tau_{mol}(\lambda) = \hat{P} \tau_m(\lambda), \quad (18)$$

where $\hat{P} = \frac{P}{P_0}$, P is the site pressure, $P_0 = 1013.25 \text{ mb}$ and $\tau_m(\lambda)$ is given by the approximate formula similar to Equation (17):

$$\tau_m(\lambda) = \tau_m(\lambda_0) \left(\frac{\lambda}{\lambda_0} \right)^{-v}. \quad (19)$$

One can assume that $\tau_m(\lambda_0) = 0.0084$ and $v = 4.0932$. Both parameters can vary depending on temperature, humidity and pressure profiles [14,17–19]. The site pressure at a given altitude H can be calculated using the following equation: $P = P_0 \exp\left(-\frac{H}{H_0}\right)$ assuming the scale height H_0 (e.g., 6 km). Alternatively, the value of $\hat{P} = P/P_0$ can be derived from the information on the atmospheric pressure P at a given location (e.g., from the European Centre for Medium-Range Weather Forecasts (ECMWF) re-analysis (<https://www.ecmwf.int/en/forecasts/datasets> (accessed on 23 March 2022))). We shall assume that the spectral aerosol asymmetry parameter is described by the following formula [7]:

$$g_{aer}(\lambda) = g_0 + g_1 e^{-\frac{\lambda}{\lambda_0}}, \quad (20)$$

where the wavelength λ is in microns and

$$g_0 = 0.5263, g_1 = 0.4627, \lambda_0 = 0.4685 \mu\text{m}. \quad (21)$$

Taking into account that the spectral TOA reflectance is determined mostly by the underlying snow reflectance for the case of a cloudless sky, we can use a simplified approximation for the aerosol phase function $p_{aer}(\theta)$ in Equation (14). This function can be calculated using Mie theory under the assumption of aerosol particle size distribution and the complex refractive index of aerosol particles or their mixture. In this work we assume that the aerosol phase function can be presented in the following analytical form [20]:

$$p_{aer}(\theta) = c p_{aer,1}(\theta) + (1 - c) p_{aer,2}(\theta), \quad (22)$$

$$p_{aer,1}(\theta) = \frac{1 - g_{aer,1}^2}{(1 - 2g_{aer,1} \cos \theta + g_{aer,1}^2)^{\frac{3}{2}}}, \quad (23)$$

$$p_{aer,2}(\theta) = \frac{1 - g_{aer,2}^2}{(1 - 2g_{aer,2} \cos \theta + g_{aer,2}^2)^{\frac{3}{2}}}.$$

We shall assume that

$$g_{aer,1} = 0.8, g_{aer,2} = -0.45. \quad (24)$$

It follows for the asymmetry parameter for the case under study:

$$g_{aer} = c g_{aer,1} + (1 - c) g_{aer,2} \quad (25)$$

and, therefore,

$$c = \frac{g_{aer} - g_{aer,2}}{g_{aer,1} - g_{aer,2}}, \quad (26)$$

where we assume that g_{aer} is given by Equation (20). This concludes the description of the approach to derive the atmospheric path reflectance.

2.3. The Atmospheric Spherical Albedo

Namely, the following expression for the atmospheric plane albedo derived using the same technique as used for the determination of the atmospheric path reflectance outlined above can be used [9].

$$r_p(\mu_0) = 1 - \frac{f(\mu_0)}{1 + 0.75(1 - g)\tau}, \quad (27)$$

where $f(\mu_0)$ is given by Equation (10) and light absorption processes are neglected. It follows from Equation (27) as $\tau \rightarrow 0$:

$$r_p(\mu_0) = w\tau, \quad (28)$$

where $w = (2\mu_0)^{-1} - 0.75g$, which is a valid approximation at small values of g . In particular, Equation (28) coincides with a similar formula given in [21,22] for the case of $g = 0$.

The spherical albedo is defined as

$$r_a = 2 \int_0^1 r_p(\mu_0) \mu_0 d\mu_0. \quad (29)$$

The substitution of Equation (27) to Equation (29) gives after integration:

$$r_a = 1 - \frac{1 + \psi(\tau)}{1 + 0.75(1 - g)\tau}, \quad (30)$$

where

$$\psi(\tau) = \left[1 + \frac{\tau}{2}\right] \frac{\tau^2}{2} E_1(\tau) - [1 + \tau] \frac{\tau}{4} \exp(-\tau) \quad (31)$$

and

$$E_1(\tau) = \int_1^{\infty} \frac{\exp(-x\tau)}{x} dx \quad (32)$$

is the exponential integral [23]. The exponential integral has the following properties [20,23]:

$$E_1(\tau \rightarrow \infty) = \exp(-\tau)/\tau \rightarrow 0, \quad (33)$$

$$\tau E_1(\tau \rightarrow 0) = \tau^2 - \frac{\tau^3}{4} + \frac{\tau^4}{18} - \frac{\tau^5}{96} - \tau \ln \tau - \gamma\tau, \quad (34)$$

where $\gamma = 0.5772157$ is the Euler's constant. Therefore, one can see that $r_a \rightarrow 1$ as $\tau \rightarrow \infty$ as it should be for nonabsorbing case considered here.

The atmospheric optical thickness is usually smaller than 0.5 for polar atmospheres and one can use the approximation given by Equation (34) for the product $\tau E_1(\tau)$ in Equation (31). Then it follows:

$$\psi(\tau) = \frac{1}{2} \left(\tau + \frac{\tau^2}{2}\right) \left(\tau^2 - \frac{\tau^3}{4} + \frac{\tau^4}{18} - \frac{\tau^5}{96} - \tau \ln \tau - \gamma\tau\right) - \frac{1}{4}(1 + \tau)\tau \exp(-\tau). \quad (35)$$

Therefore, one derives:

$$r_a = 1 - \left[\frac{1 - \frac{\tau}{4}(1 + \tau) \exp(-\tau) + \frac{\tau^2}{2} \left(1 + \frac{\tau}{2}\right) \left(\tau - \frac{\tau^2}{4} + \frac{\tau^3}{18} - \frac{\tau^4}{96} - \ln \tau - \gamma\right)}{1 + 0.75(1 - g)\tau} \right]. \quad (36)$$

It follows from Equation (36) as $\tau \rightarrow 0 : r_a \rightarrow b\tau$, where $b = 1 - 3g/4$. One can see that $r_a \approx \tau$ at small values of atmospheric optical thickness and $g = 0$. The value of $r_a < \tau$ at $g > 0$.

The intercomparison of the dependence of spherical albedo on the value of atmospheric optical thickness derived using Equation (36) and the exact radiative transfer calculations is shown in Figure 1, where we also present the results derived using the following simple formula (approximation—2) valid for the case of pure molecular scattering [24]:

$$r_a = \tau(a \exp(-\tau/\alpha) + b \exp(-\tau/\beta) + c) \quad (37)$$

where $a = 0.180$, $b = 0.583$, $c = 0.215$, $\alpha = 0.168$, $\beta = 1.092$. The maximal error of Equation (37) is smaller than 1%. It is based on the parameterisation of exact radiative transfer (RT) calculations for the case of molecular scattering [24]. The error of approximation (36) is smaller than 2% at $\tau \leq 1$ for the molecular scattering case. We also show the calculations for the case of aerosol and molecular scattering mixture. It is assumed that aerosol optical thickness is 0.05 and molecular optical thickness changes from 0.01 to 1.0. The aerosol parameters were taken from [25]. One can see that the errors of the approximation do not increase substantially in the presence of a thin aerosol layer. It should be pointed out that one is interested not in the value of r_a but rather in the quantity $\gamma = (1 - r_a r_s)^{-1}$ in the problem under study (see Equation (2)). The error of an approximation for the value of γ is even lower.

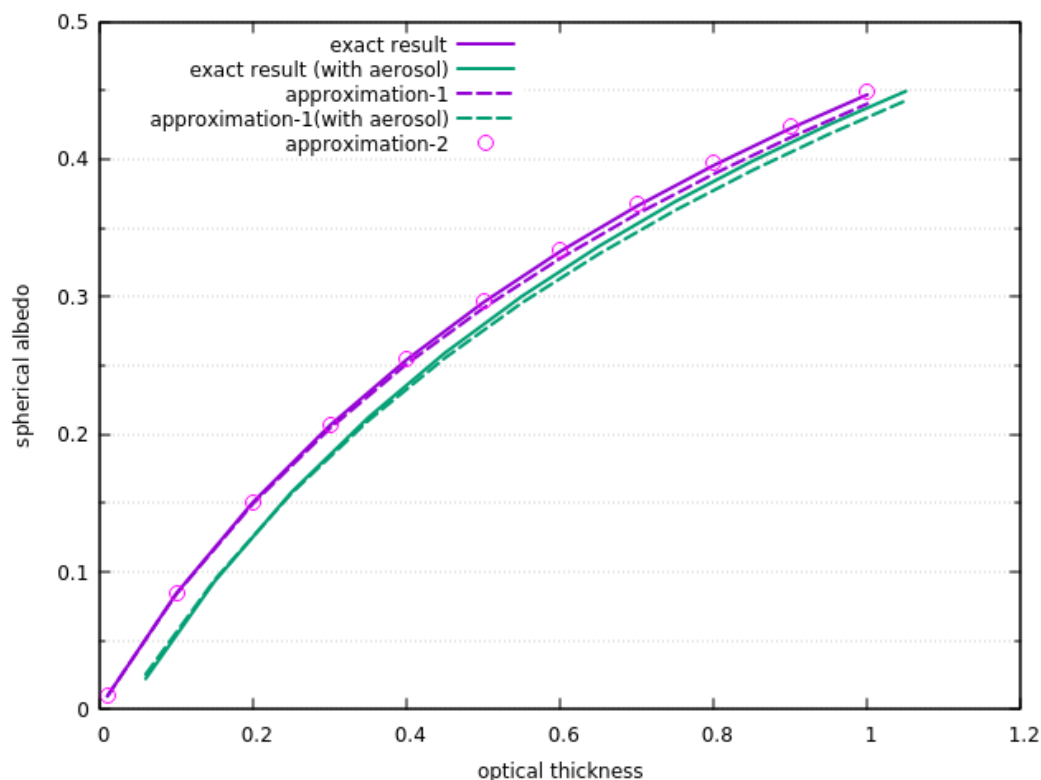


Figure 1. The intercomparison of different approximations for the calculation of the spherical albedo of atmosphere with molecular scattering with different values of atmospheric optical thickness. The exact RT calculations have been performed using the SORD code [26].

2.4. The Atmospheric Transmittance Outside Gaseous Absorption Bands

The transmission function T_a is approximated as follows [10]:

$$T_a = t_a^m, \quad (38)$$

where m is given by Equation (6). The value of t is calculated using the following approximation [10]:

$$t_a = e^{-B\tau}. \quad (39)$$

Here,

$$B = \frac{1}{2} \int_{\frac{\pi}{2}}^{\pi} p(\theta) \sin\theta \, d\theta \quad (40)$$

is the so-called backscattering fraction. The substitution of Equation (14) to Equation (40) gives:

$$B = \frac{\tau_{mol} B_{mol} + \tau_{aer} B_{aer}}{\tau_{mol} + \tau_{aer}} \quad (41)$$

where $B_{mol} = 0.5$,

$$B_{aer} = cB(g_{aer,1}) + (1 - c)B(g_{aer,2}) \quad (42)$$

and

$$B(G) = \frac{1 - G}{2G} \left[\frac{1 + G}{\sqrt{1 + G^2}} - 1 \right] \quad (43)$$

It follows at small values of G :

$$B(G) \approx \frac{1}{2} + \frac{G(G^2 - 3)}{2(1 + G^2 + (1 - G^2)\sqrt{1 + G^2})}. \quad (44)$$

The accuracy of Equations (38)–(40) has been studied in [10], where it has been found this approximation can be used with an accuracy better than 5% at solar zenith angles smaller than 70 degrees for the continental and water soluble aerosol layers with an aerosol optical thickness smaller than 0.5, which is the case for polar atmospheres.

2.5. The Atmospheric Gaseous Transmittance

Atmospheric gaseous transmittance in Equation (2) can be presented as a product of transmittances due to various gaseous components in the atmosphere. In this work, we are interested primarily in the calculation of radiative characteristics in the range 400–1000 nm, where the main atmospheric gases which contribute significantly to the atmospheric absorption processes, are molecular oxygen, ozone, and water vapor. Therefore, to simplify the calculations, the contribution of other gases is ignored. Such an approach has been also used in several previous papers on the subject [2,11]. In particular, we shall assume that the gaseous transmittance is given by the following product:

$$T_g = T_{O_2} T_{O_3} T_{H_2O}, \quad (45)$$

where T_{O_2} , T_{O_3} , and T_{H_2O} are the gaseous transmittances due to molecular oxygen, ozone and water vapor.

2.5.1. Ozone

We shall assume that the ozone transmittance T_{O_3} can be derived using the following expression [17,27]:

$$T_{O_3} = \exp(-m_{O_3} \tau_{O_3}(\lambda)), \quad (46)$$

where m_{O_3} is the ozone airmass factor (AMF) and $\tau_{O_3}(\lambda)$ is the vertical optical density (VOD) of ozone:

$$\tau_{O_3}(\lambda) = \int_0^{z_{top}} C_{abs,O_3}(\lambda, z) n_{O_3}(z) dz, \quad (47)$$

where $C_{abs,O_3}(\lambda, z)$ is the ozone absorption cross-section, z is the altitude, z_{top} is the top of atmosphere altitude, $n_{O_3}(z)$ is the number concentration of ozone molecules at the altitude z .

We use the geometrical approximation for the AMF (see Equation (6)). In the spectral region of interest, the dependence of the ozone absorption cross section on both temperature and pressure (and, therefore, the altitude) can be ignored. Then one derives from Equation (47):

$$\tau_{O_3}(\lambda) = NC_{abs,O_3}(\lambda), \quad (48)$$

where

$$N_{O_3} = \int_0^{z_{top}} n_j(z) dz \quad (49)$$

is the total ozone column (TOC) measured in molecules per cm^2 . The value of C_{abs,O_3} is measured in cm^2 (per molecule) and can be parameterised as follows in the spectral range under study [28]:

$$C_{abs,O_3}(\lambda) = AF(\lambda), \quad (50)$$

where $A = 18.48 \times 10^{-21} \text{cm}^2/\text{molecule}$

$$F(\lambda) = \frac{\zeta(\lambda)}{(1 + \zeta(\lambda))^2}, \quad (51)$$

$$\zeta = \exp\left(\frac{w(\lambda) - w_p}{\Delta}\right), \quad (52)$$

$w = 10^7/\lambda$, where λ is given in nm and w is the wavenumber with the dimension cm^{-1} . The authors of [28] suggest (after correction of a misprint) the following values for the parameters in Equation (52): $w_p = 16811 \text{cm}^{-1}$, $\Delta = 877 \text{cm}^{-1}$ (at wavenumbers $w < w_p$) and $\Delta = 1210 \text{cm}^{-1}$ at $w \geq w_p$. We show the results of calculations of $C_{abs,O_3}(\lambda)$ according to this equation and also measurements of C_{abs,O_3} [29] in Figure 2a as the function of the wavelength $\lambda = 10^7/w$, where w is given in $1/\text{cm}$ and the dimension of the wavelength is nm. One can see that theoretical and experimental results differ in the regions, where the spectral curve $C_{abs,O_3}(\lambda)$ has oscillations. The relative accuracy is better than 25% in the spectral range 500–700 nm (see Figure 2b), which suits our purposes (especially because we are interested in the value of $\exp(-m\tau_{O_3})$, which is derived with much better accuracy as compared to the ozone VOD). Summing up, we assume that the value of T_{O_3} can be approximated as follows:

$$T_{O_3} = \exp(-\kappa F(\lambda)), \quad (53)$$

where $\kappa = Am_{O_3}N_{O_3}$. The error of the ozone transmittance calculation using simple Equation (53) as compared to the case, where experimental values of C_{abs,O_3} are used, is shown in Figure 3 at $N_{O_3} = 300 \text{DU}$ ($1 \text{DU} = 2.69 \times 10^{16}$ ozone molecules/ cm^2) and the ozone airmass factor $m_{O_3} = 1$. One can see that the respective error is below 1% for the case studied, which is smaller than the error of the respective spectral reflectance measurements.

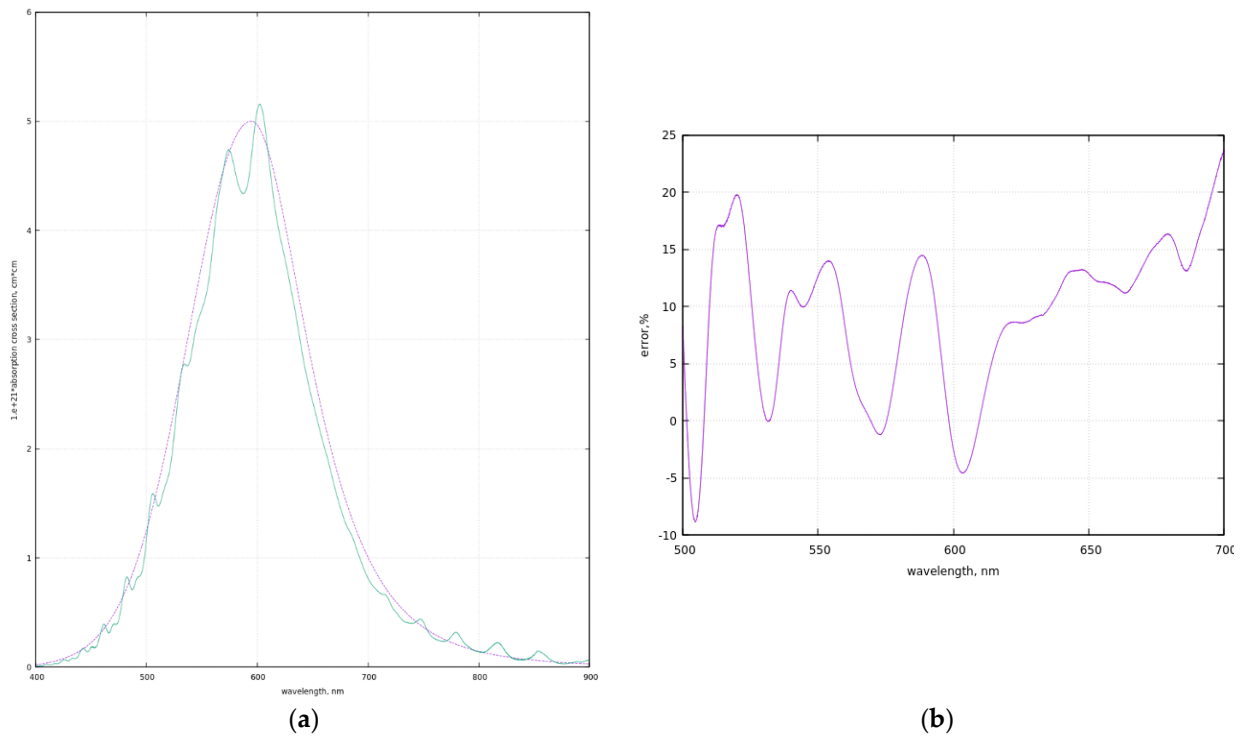


Figure 2. (a) The intercomparison of modelled (dashed) and experimentally measured (solid line) ozone absorption cross section (at temperature $t = 233$ K). (b) The error of the approximation for the ozone VOD.

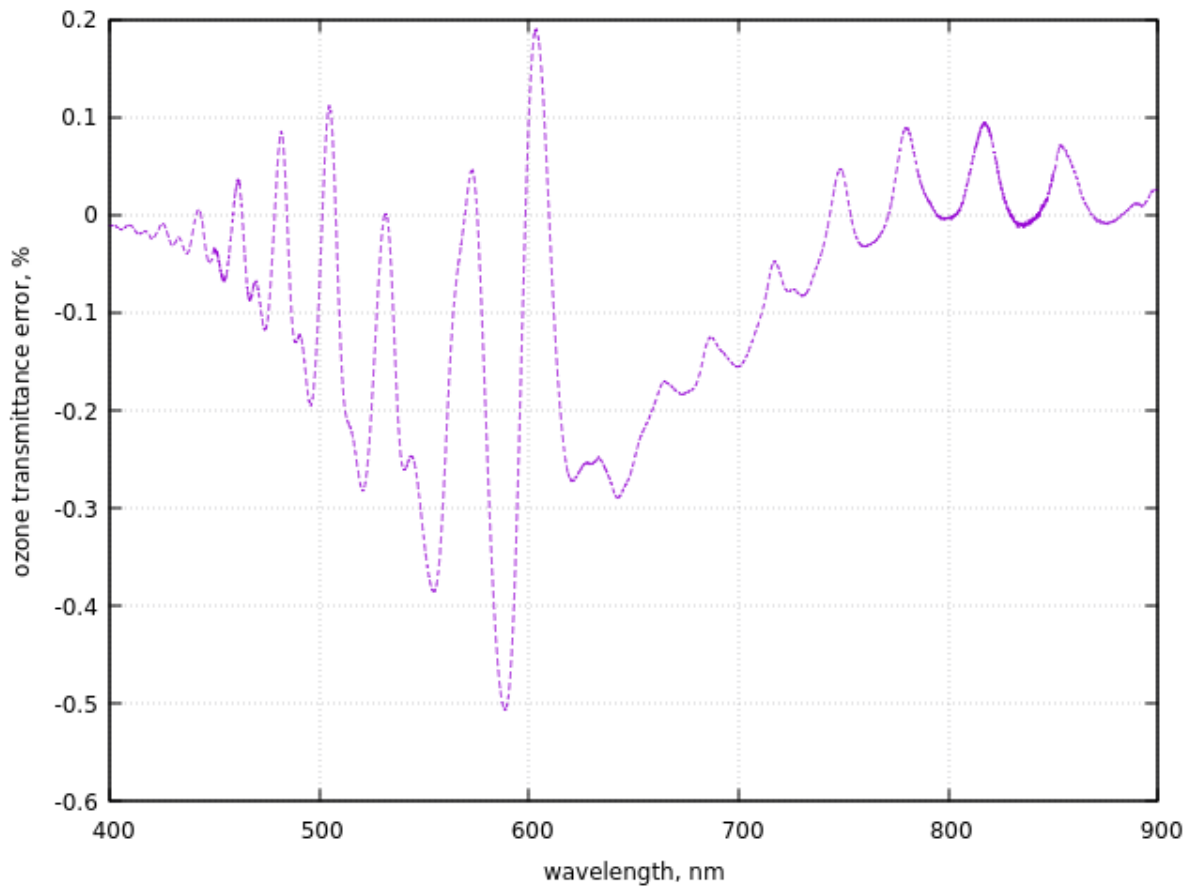


Figure 3. The ozone transmittance error.

2.5.2. Water Vapor

The transmittance of water vapor in the spectral range 900–1000 nm can be calculated using the following simple equation [28]:

$$T_{H_2O} = \exp\{-s^{x_1}\}, \quad (54)$$

where

$$s = N_{H_2O}^{ef} c_{H_2O}(\lambda), \quad (55)$$

$$N_{H_2O}^{ef} = Q_{H_2O} m_{H_2O} N_{H_2O}, \quad (56)$$

$$Q_{H_2O} = (\bar{P}/P_0)^n (t_0/\bar{t})^k, \quad (57)$$

$$c_{H_2O}(\lambda) = \sum_{j=1}^2 B_j F_j(\lambda), \quad (58)$$

$$F_j(\lambda) = \frac{\zeta_j(\lambda)}{(1 + \zeta_j(\lambda))^2} \tilde{\zeta}_j(\lambda) = \exp\left(\frac{w(\lambda) - w_j}{\Delta_j}\right), \quad (59)$$

$w = 10^7/\lambda$, where λ is given in nm and w is the wavenumber with the dimension cm^{-1} , $n = 0.775$, $k = 0.721$, $t_0 = 273.16$ K, $P_0 = 1013.25$ hPa, (\bar{P}, \bar{t}) are average values of pressure and temperature for a given location calculated using respective vertical profiles, $x_1 = 0.649$; m_{H_2O} is the water vapor air mass factor, which can be found using geometrical approximation (see Equation (6)). The constants B_j , w_j and Δ_j are given in Table 1 below. The value of the Precipitable Water vapor (PWV) content N_{H_2O} , which is the input parameter for the model, is given in cm. When measured in linear units (cm, mm), the water vapor column is represented by the height (or depth) N_{H_2O} that the water column would occupy if the vapor were condensed into liquid and spread evenly across the column. Using the density of water, we can also report water vapor in $\text{gcm}^{-2} = 1$ cm or $\text{kgm}^{-2} = 1$ mm. The example of water vapor gaseous transmittance calculated in the framework of this model is presented in Figure 4.

Table 1. The parameters of water vapor absorption model [28].

λ , nm	B_j , cm^{-1}	w_j , cm^{-1}	Δ_j , cm^{-1}	Comment
910 ($j = 1$)	0.744	11,099	23.4 ($w < w_j$) 73.8 ($w \geq w_j$)	Weak absorption band
940 ($j = 2$)	7.560	10,697	23.1 ($w < w_j$) 110.2 ($w \geq w_j$)	Strong absorption band

Equation (54) is similar to Equation (53) except x_1 and Q differ from the unity as assumed in Equation (54). This difference is due to the fact that most of the ozone is located in a single layer positioned in the stratosphere, which is not the case for water vapor with the largest concentrations closer to the surface. The value of the effective PWV content $N_{H_2O}^{ef}$ can be estimated from Equations (56) and (57) under the assumption that the value of Q_{H_2O} is known. The determination of N_{H_2O} requires information on water vapor air mass factor and also temperature and pressure profiles for a given location.

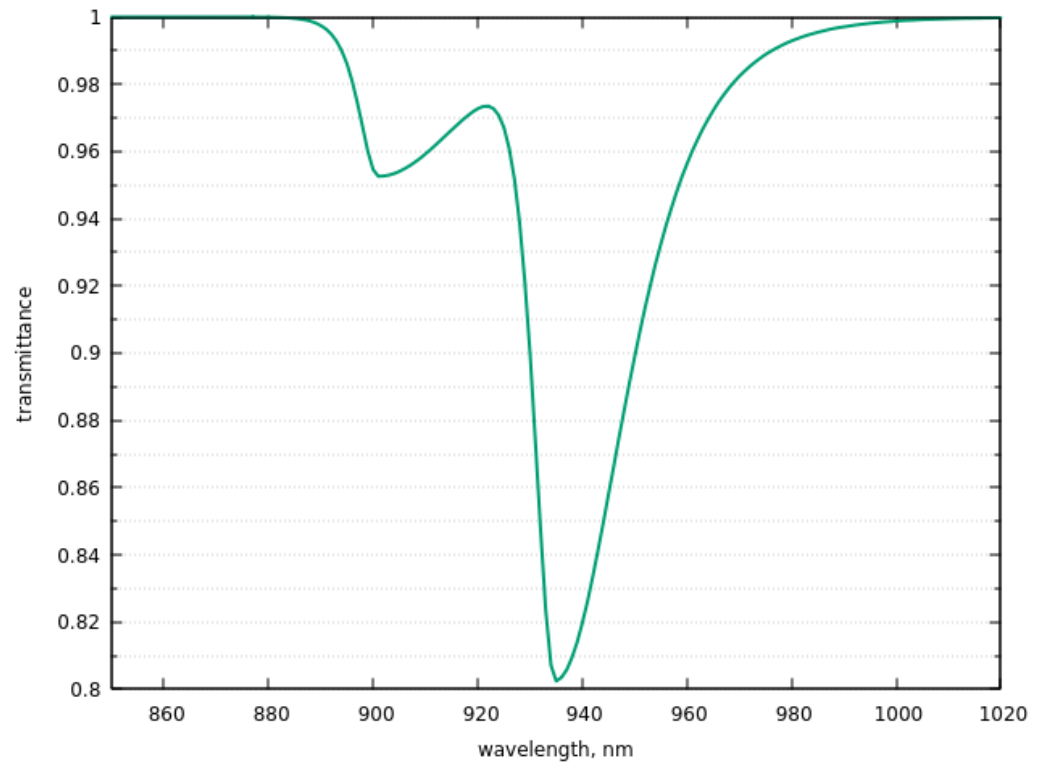


Figure 4. Water vapor transmittance at $N_{H_2O} = 0.33 \text{ mm}^{-1}$, $\bar{T} = 233 \text{ K}$, $\bar{P} = 325 \text{ hPa}$, $m_{H_2O} = 3.32$.

2.5.3. Oxygen

The oxygen transmittance is found using the approximation similar to Equation (54) [30]:

$$T_{O_2} = \exp(-s^{x_2}), \quad (60)$$

where

$$s = N_{O_2}^{ef} c_{O_2}(\lambda), \quad (61)$$

$$N_{H_2O_2}^{ef} = Q_{O_2} m_{O_2} N_{O_2}. \quad (62)$$

The parameter Q_{O_2} is given by formula similar to Equation (57) except $n = 0.9353$, $k = 0.1936$, m_{O_2} is the oxygen AMF, which can be estimated using geometrical approximation (see Equation (6)), N_{O_2} is the oxygen amount in atm-cm, $x_2 = 0.5641$.

The spectral function $c_{O_2}(\lambda)$ has been tabulated in [30]. We have parameterised this function using the double Gauss approximation (at the wavelengths smaller or equal to 764 nm):

$$c_{O_2}(\lambda) = \Lambda \exp(-1.7(\lambda - \lambda_1)^2) + 0.32\Lambda \exp(-0.7(\lambda - \lambda_2)^2), \quad (63)$$

where $\lambda_1 = 760.75 \text{ nm}$, $\lambda_2 = 763.36 \text{ nm}$, $\Lambda = 1.8 \times 10^{-5} (\text{cm} - \text{atm})^{-1}$ and λ is expressed in nm. At the wavelengths λ larger than 764 nm, the following parameterisation has been used:

$$c_{O_2}(\lambda) = \frac{Y}{1 + \exp[(\lambda - \lambda_s)/\Delta_s]}, \quad (64)$$

where $Y = 8.419 \times 10^{-6} (\text{cm} - \text{atm})^{-1}$, $\lambda_s = 764.11 \text{ nm}$, $\Delta_s = 0.85036 \text{ nm}$. The intercomparison of $c_{O_2}(\lambda)$ derived using Equations (63), (64) and data presented in [30] is shown in Figure 5. It follows that the proposed parameterisations can indeed be used to model gaseous transmittance in the molecular oxygen A-band. The transmittance $T_{O_2}(\lambda)$ at $N_{O_2} = 8.706853 \times 10^5 \text{ cm-atm}$ and $m_{O_2} = 1$ is given in Figure 6 both using Equations (63) and (64), and tabular data for the spectral function given in [30]. Good correspondence between the two approaches for the calculation of $T_{O_2}(\lambda)$ is found.

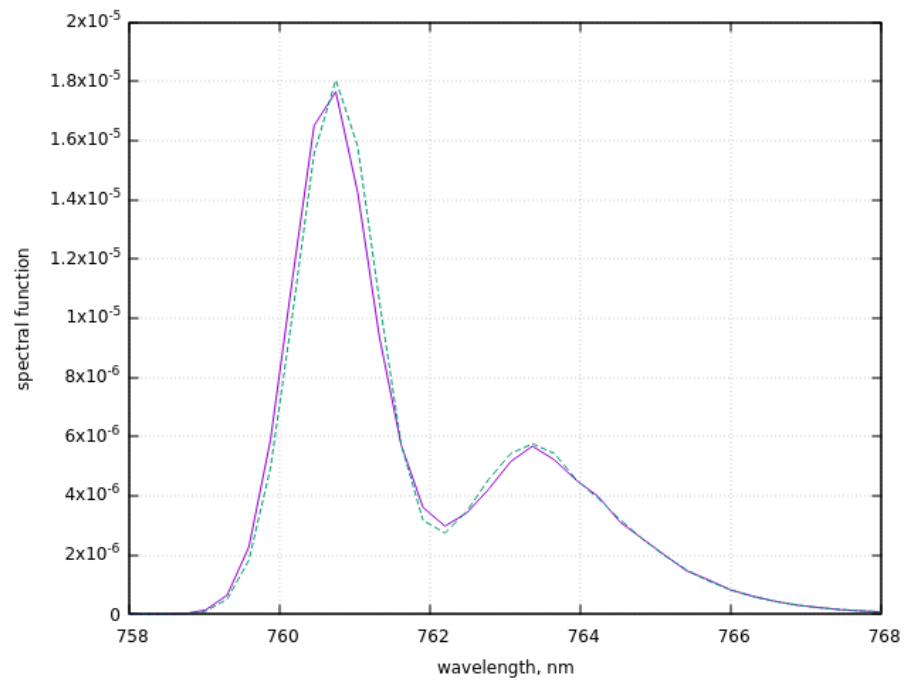


Figure 5. The spectral function tabulated in [30]) (solid line) and derived using Equations (63) and (64) (dashed line).

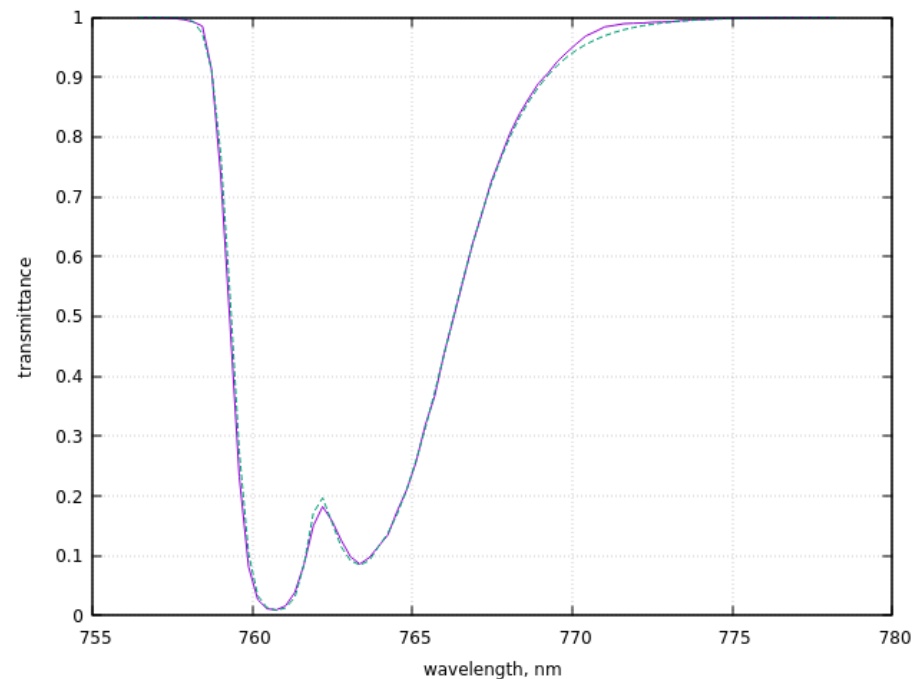


Figure 6. The oxygen transmittance (solid line—the tabular data given in [30] are used, dashed line—Equations (63) and (64) for the spectral function are used).

2.6. Reflectance of Solar Light from a Snow Surface

The only function in Equation (2), which we did not study so far is the spectral snow reflectance $R_s(\lambda)$. It is modelled using the approximation proposed in [31–35] for the case of a clean vertically and horizontally homogeneous plane—parallel layers of turbid media:

$$R_s(\mu, \mu_0, \varphi) = R_0(\mu, \mu_0, \varphi) r_s^{\xi}, \quad (65)$$

where

$$\zeta = u(\mu_0)u(\mu)/R_0(\mu, \mu_0, \varphi), \quad (66)$$

$$u(\mu_0) = \frac{3}{5}\mu_0 + \frac{1 + \sqrt{\mu_0}}{3}, \quad (67)$$

$$r_s = \exp\{-\sqrt{y}\}, \quad (68)$$

$$y = L\alpha_i, \quad (69)$$

$$R_0 = \frac{a + b(\mu_0 + \mu) + c\mu_0\mu + p_s(\theta)}{4(\mu_0 + \mu)}, \quad (70)$$

where $a = 1.247$, $b = 1.186$, $c = 5.157$, $\alpha_i = \frac{4\pi\chi}{\lambda}$ is the bulk ice absorption coefficient, χ is the imaginary part of the complex ice refractive index [5], and L is the effective absorption length (proportional to the average ice grain size). The phase function of a snow layer $p_s(\theta)$ is approximated as [5,6]:

$$p_s(\theta) = 11.1 \exp(-0.087\theta) + 1.1 \exp(-0.014\theta), \quad (71)$$

where θ is the scattering angle in degrees. Equation (65) follows from the analysis of the radiative transfer equation valid at the snow single scattering albedo ω close to one, which is a valid approximation in the spectral range under study [5]. Additionally, it is assumed that $1 - \omega$ is proportional to the product of the snow grain size and the bulk ice absorption coefficient and the snow phase function does not change considerably in the visible and near infrared regions of the electromagnetic spectrum [5].

In the case of polluted snow, the equations given below remain valid except the parameter y is changed to the following expression [33,35]:

$$y = L \left[\alpha_i + f(\lambda/\lambda_0)^{-v} \right], \quad (72)$$

where v is the absorption Angström parameter of impurities in snow, $\lambda_0 = 1 \mu\text{m}$ and f is the parameter, which is proportional to the relative impurity concentration $C = C_{imp}/C_{ice}$, where C_{imp} is the volumetric concentration of impurities, C_{ice} is the volumetric concentration of ice grains. Namely, it follows [35]:

$$f = \frac{C}{K}\kappa_0 \quad (73)$$

where K is the absorption enhancement parameter (≈ 1.8) and κ_0 is the volumetric absorption coefficient of impurities at the wavelength $1 \mu\text{m}$. The value of κ_0 is equal to the ratio of the average absorption cross-section of impurities (say, dust particles) to their average volume [35]. One can see that the description of optical characteristics of polluted snow requires two additional parameters (f, v).

3. The Intercomparison of Derived Parameterisation with Spaceborne Measurements of Spectral Top-of-Atmosphere Reflectance

The TOA spectral reflectance function calculated using Equation (2) is given in Figure 7. We also show the simulation and measurement results for the top-of-atmosphere OLCI (<https://sentinels.copernicus.eu/web/sentinel/technical-guides/sentinel-3-olci> (accessed on 18 September 2022)) reflectance at Dome C in Antarctica. The specification of both OLCI channels and their widths is used in the averaging procedure (assuming box function). The derived bottom of atmosphere (BOA) snow reflectance is also shown for comparison. The TOA reflectance measured by OLCI is given by crosses in Figure 7. The assumed parameters of the atmosphere—underlying snow system are given in Table 2. The molecular optical thickness has been modelled using the following equation:

$$\tau_{mol} = 0.015 + 20.64 \exp(-\lambda/86.16), \quad (74)$$

where λ is the wavelength in nm. Equation (74) has been derived by fitting the spectral molecular optical thickness tabular data provided in [14] for the case of the Antarctica Dome C conditions.

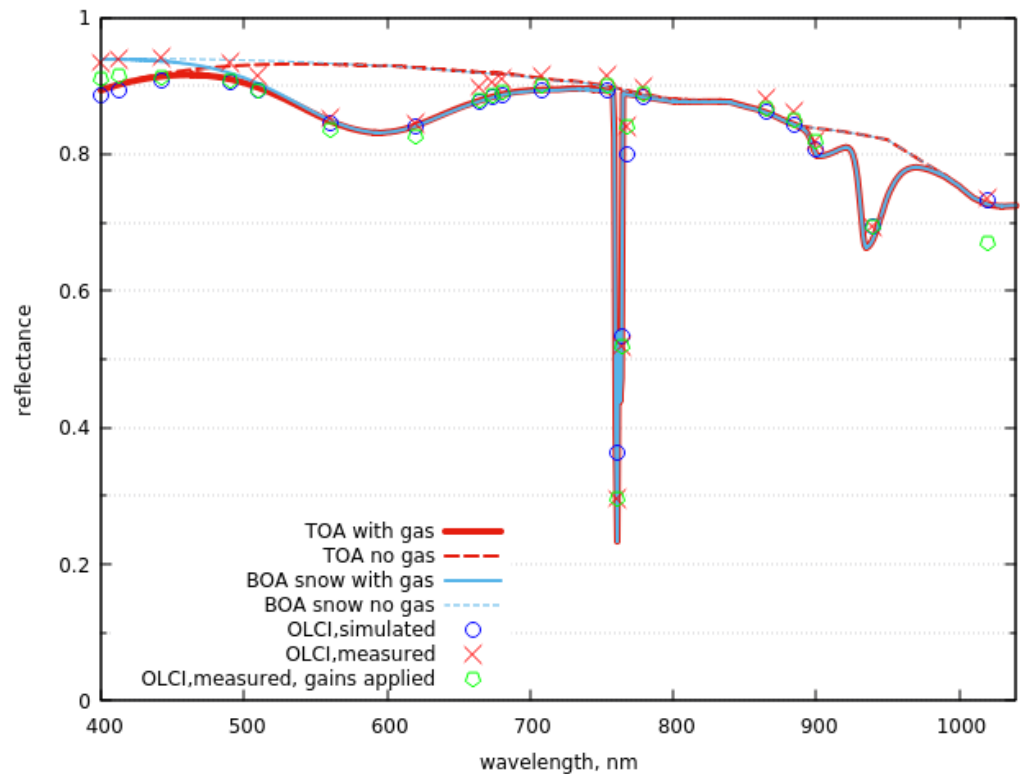


Figure 7. The spectral TOA reflectance measured by OLCI (symbols) and also modelled using Equation (2) (solid red line). Dashed red line corresponds to the artificial atmosphere without gas. Blue dashed line corresponds to the case when atmospheric contribution is neglected. Solid blue line corresponds to the case when absorption by atmospheric gases (but not light scattering in atmosphere) is fully accounted for. The solar zenith angle is equal to 63.61 degrees, the VZA is 20.63 degrees and the relative azimuthal angle is 118.39 degrees. The satellite measurements have been performed on November 10, 2017, at Dome C (Antarctica) under geometry specified above.

Table 2. The parameters of the model used in Figure 7 for the case of clean snow underlying surface.

N	Parameter	Value	Comment
1	α	0.008	atmospheric aerosol
2	β	1.3	atmospheric aerosol
3	N_{O_2} , cm-atm	8.706853×10^4	oxygen
4	N_{O_3} , DU	250	ozone
5	N_{H_2O} , mm	0.33	water vapor
6	P , hPa	650	surface pressure
7	\bar{P} , hPa	325	average pressure
8	\bar{t} , K	233	average temperature
9	L , mm	2.24	snow effective absorption length

The spectral imaginary part of the ice refractive index has been found as proposed in [5] using the dataset presented in [36] at wavelengths below 600 nm and that given in [37] at larger wavelengths. The linear interpolation has been applied to derive the values between the spectral grid points presented in respective tables.

Figure 7 shows that OLCI spectra are significantly influenced by the gaseous absorption (see, e.g., the oxygen absorption band located around 761 nm). The decrease in OLCI spectra towards 400 nm is due to atmospheric light scattering. This decrease can be used to estimate the atmospheric aerosol load over snow for elevated atmospheric aerosol load conditions. As a matter of fact, the aerosol load in Antarctica is in general too low [15] to be measured from a satellite taking into account instrument calibration errors and inaccuracy of bottom-of-atmosphere albedo estimations. The influence of atmospheric scattering can be neglected at wavelengths above 500 nm for the case studied. Measurements at 1020 nm are affected by the light absorption effects in snow cover with larger values of reflectance for smaller and less absorbing ice grains. Measurements in the vicinity of ozone (600 nm) and water vapor (940 nm) absorption bands can be used to estimate the total ozone and the atmospheric precipitable water vapor content. They can be derived from the depth of corresponding absorption bands as seen in the reflected light [5,38]. The atmospheric oxygen column is known in advance for any height of the underlying surface. Therefore, the measurements of reflectance in the oxygen A-band can be used to estimate the height of the underlying surface, and ground atmospheric pressure and develop various cloud screening procedures.

We have found that the difference between theoretical results derived using Equation (2) and observations for all channels is smaller than 5% except for the channel corresponding to the maximal absorption by oxygen in the OLCI spectrum, where one needs to use the instrument spectral response function (instead of box function) in the averaging procedure. It should be pointed out that some differences seen in Figure 7 are due to errors in OLCI measurements. In particular, theoretical results suggest that the spectral reflectance must decrease in the range of 400–450 nm (towards a shorter wavelength). This is mostly due to molecular light scattering effects for the case studied. Such a decrease is not seen in the OLCI spectrum given in Figure 7 by red crosses, which makes it possible to suspect the problem with OLCI measurements in this spectral range. As a matter of fact, such an anomaly in OLCI spectra has already been detected. In particular, the use of OLCI calibration coefficients (gains), which leads to a decrease in OLCI reflectance in the range of 400–450 nm and a change in OLCI spectral reflectance at some other channels, have been elaborated in [39]. As it follows from Figure 7, the difference between the modelled and measured spectra decreases after the application of gains (except for the last channel). The difference at the last OLCI channel is due to the fact that the value of L in Table 2 has been derived from OLCI measurements without the application of gains. This difference is reduced in case the value of L is retrieved from the measurements at the last OLCI channel after the application of the gains.

The total ozone column and precipitable water vapor content are also important atmospheric parameters, which can be found. It follows that the value of $\text{TOC} = 250$ DU for the case shown in Figure 7. ECMWF data for DOME C provided in OLCI files at this date and time give $\text{TOC} = 291$ DU. Therefore, the difference is around 14% for the TOC for the case studied. The study of errors related to the determination of TOC from OLCI measurements has been performed in [27]. The derived value of PWV for the case shown in Figure 7 is 0.33 mm. This value is close to the average value of PWV at the site for autumn ($\text{PWV} = 0.4$ mm), where averaging has been performed for 4 years (2010–2014, see Table 4 presented in [40]). Further discussion of the PWV content as retrieved using OLCI over land surfaces and related errors including the influence of instrumental effects on the retrieval is given in [38].

As a matter of fact, the theory presented above makes it possible to estimate the product $X = mQN$ accurately. The correct value of N can be derived from X : $N = X/Qm$ using improved estimation of the AMF m and also the parameter Q . Further discussion of this topic is out of the scope of this paper.

The effective grain size can be derived from the value of the effective absorption length using the following approximate equation [41]: $d = L/16$. Therefore, the effective grain

diameter $d = 0.14$ mm for the case shown in Table 2, which is consistent with grain size measurements in Antarctica as reported in [42].

We also applied the theory described above to a large OLCI dataset in Eastern Antarctica. Figure 8 shows the distribution of the coefficient of variance (normalised root-mean-square difference between model and spaceborne measurements of TOA reflectance outside the oxygen absorption band):

$$CV = \frac{RMSD}{\bar{R}}, \quad (75)$$

where

$$RMSD = \sqrt{\frac{\sum_{j=1}^J (R_{appr}(\lambda_j) - R_{meas}(\lambda_j))^2}{J}}, \quad (76)$$

$$\bar{R} = \frac{\sum_{j=1}^J R_{meas}(\lambda_j)}{J} \quad (77)$$

and $J = 18$ (oxygen absorption A-band measurements are excluded). As it follows from the comparison of Figures 8 and 9, the largest values of CVs are correlated with the largest values of OLCI reflectance in the oxygen A-band signifying the presence of clouds [43]. The parameters $L, N_{O_3}, N_{H_2O}^{ef}$ for the OLCI scene studied have been estimated using the following equations, which follow from Equations (2), (46), (54) and (65) under the assumption that the atmospheric scattering contribution is neglected [34,37]:

$$L = \frac{\ln^2(R_0/R_{21})}{\alpha_{21}\zeta^2}, \quad (78)$$

$$N_{O_3} = K \frac{\ln(R_{s,7}/R_7)}{m_{O_3}}, \quad (79)$$

$$N_{H_2O}^{ef} = \ln^\varepsilon(R_{s,20}/R_{20}), \quad (80)$$

where $K = 9349.3$ DU, $\varepsilon = 1/x_1$, $\alpha_{21} = \frac{4\pi\chi_{21}}{\lambda_{21}}$ is the bulk ice absorption coefficient 1020 nm, χ_{21} is the imaginary part of the ice refractive index at the OLCI channel $\lambda_{21} = 1020$ nm, ζ is given by Equation (66), R_7, R_{20}, R_{21} are the OLCI TOA measurements at the wavelengths 620, 940 and 1020 nm, respectively, $R_{s,7}, R_{s,20}, R_{s,21}$ are the estimated OLCI TOA reflectances at the OLCI channels 7 (620 nm), 20 (940 nm) and 21 (1020 nm). Air mass factors in Equations (79) and (80) are estimated using the geometrical approximation (see Equation (6)). The value of molecular optical thickness has been modelled using Equation (74). The imaginary part of the ice refractive index has been found as specified above. The parameter $N_{O_2}^{ef}$ has been estimated using the formula similar to Equation (80) except OLCI measurements and snow reflectance at the channel 764.38 nm have been used. Other parameters have been selected as specified in Table 2.

To increase the accuracy of the derived spectral reflectance one can substitute the approximate value of R_0 by that estimated from OLCI measurements [34]:

$$R_0 = R_{meas}^z(865 \text{ nm}) R_{meas}^{1-z}(1020 \text{ nm}), \quad (81)$$

where $z = (1 - b)^{-1}$, $b = \sqrt{\frac{\alpha_{17}}{\alpha_{21}}}$, α_{17} is the bulk ice absorption coefficient at channel 17 of OLCI (865 nm), R_{meas} is the measured OLCI reflectance at a given OLCI channel.

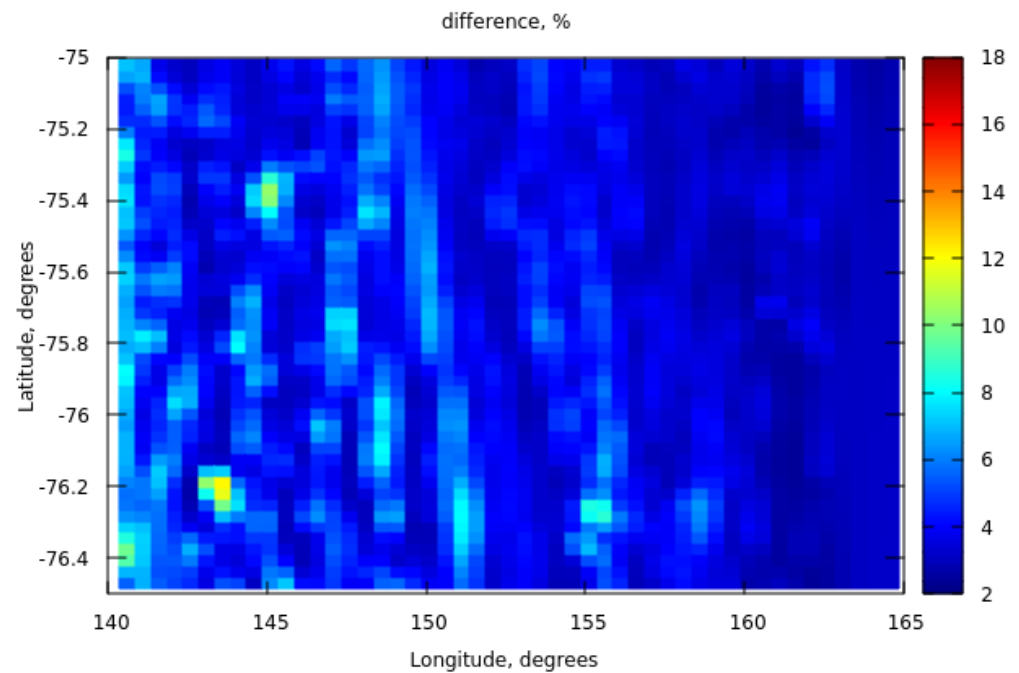


Figure 8. The difference (in percent, see Equation (75)) between measured and modelled spectra.

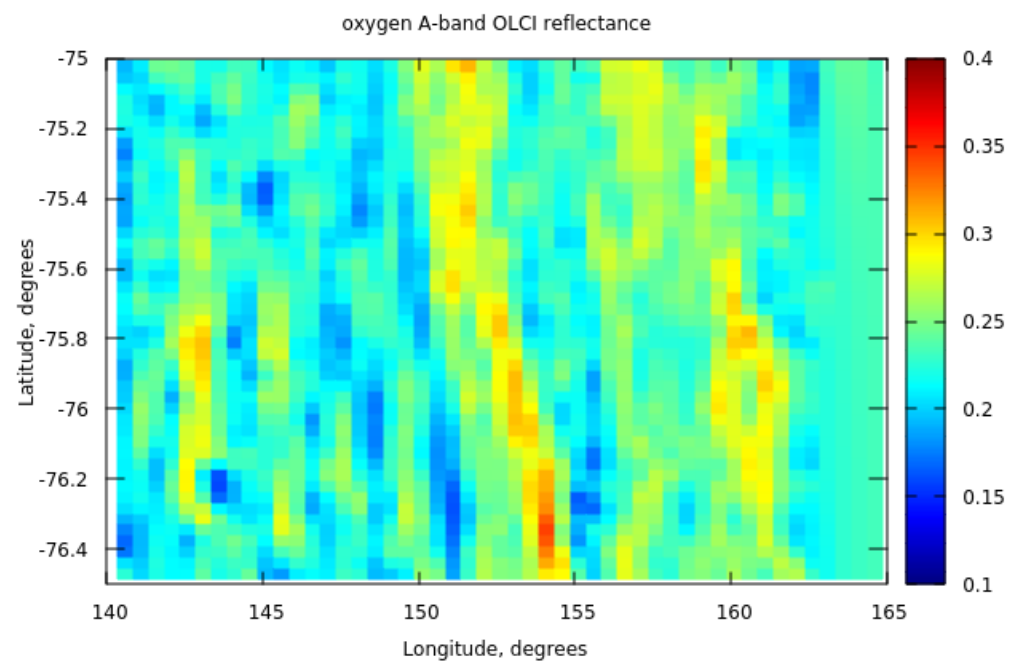


Figure 9. OLCI reflectance at 761.25 nm for the case shown in Figure 8.

The histogram of the coefficient of variance corresponding to the data shown in Figure 8 is given in Figure 10. We see that the values of CV are smaller than 10% for most cases. There are regions in Eastern Antarctica, where the deviations are below 5%. The areas with larger deviations could be due to the presence of clouds or structures on the snow surface not captured by the proposed model. The differences can be further decreased if OLCI gains are used as discussed above.

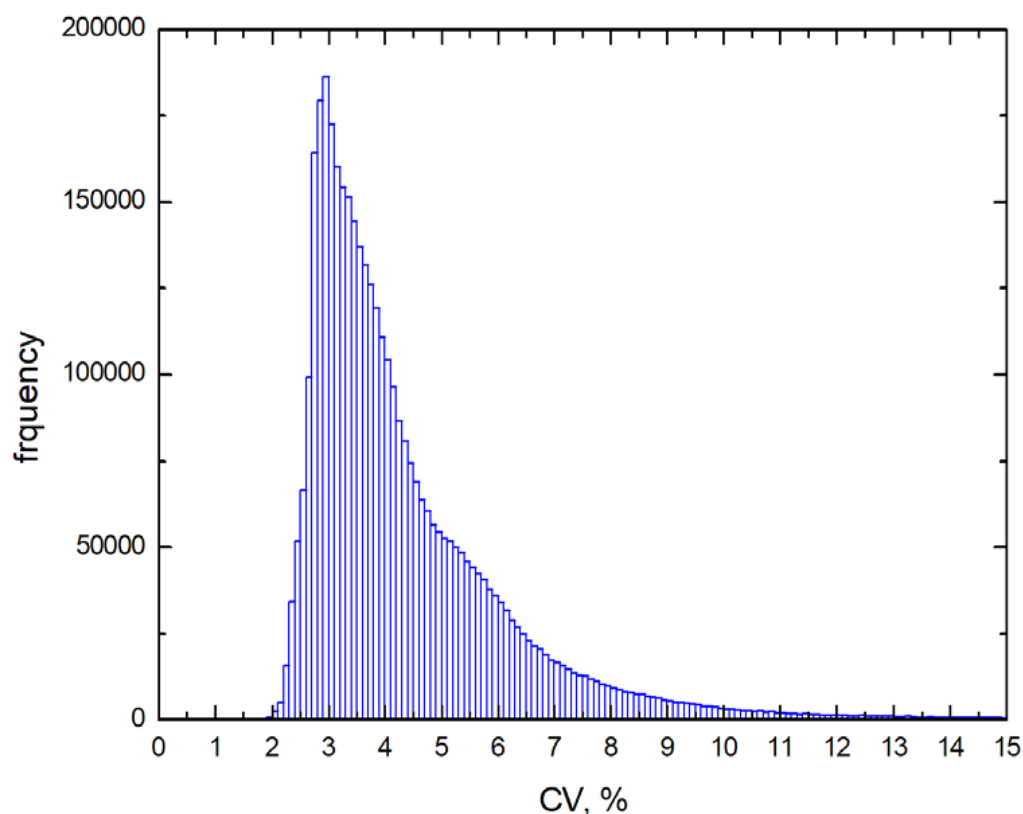


Figure 10. The statistical distribution of the coefficient of variance.

4. Conclusions

In this work, we have proposed an analytical approximation for the clear sky top-of-atmosphere spectral reflectance as measured by satellite instrumentation at a moderate spectral resolution in the visible and near-infrared regions of the electromagnetic spectrum (400–1000 nm) over extended snow surfaces, such as those existing in Antarctica. Both the atmosphere and surface are relatively clean in Antarctica, which makes the solution to the studied problem possible. One can also apply the technique to other similar areas with underlying snow and ice surfaces (e.g., Greenland, Tibetan Plateau, etc.). Although the numerical solution of the radiative transfer equation leads to more accurate results as compared to those presented in this work, it does not mean that this results in better accuracy as compared to the experimental measurements of spectral reflectance. This is related to the fact that exact modelling of light reflectance from natural snow and ice surfaces as detected on a satellite is hardly possible because of the various structures on the snow surfaces (e.g., sastrugi), close-packed media effects, layered nature and complex microstructure of snow fields containing both external and internal impurities. The technique can be extended to larger wavelengths taking into account other absorption bands of atmospheric gases. Additionally, Mie calculations [44] or look-up tables can be used for the spectral aerosol phase function and optical thickness in case the atmospheric aerosol load is substantial and the aerosol parameters are known in advance.

The spectral range 400–1000 nm is of special importance because the TOA reflectance is more sensitive to both snow and atmospheric aerosol properties as compared to longer wavelengths, where the contribution of atmospheric aerosol and molecular light scattering can be neglected and the reflectance of light from snow decreases. The fast radiative transfer FORTRAN code for the calculation of the reflectance over snow (SNOWTRAN) can be freely downloaded from the site <https://sites.google.com/site/kokhanovsky2016/codes> (accessed on 18 September 2022).

Funding: This research was funded by the European Space Agency (the EO Science for Society ESRIN CCN 4000125043/18/I-NB).

Acknowledgments: The author is grateful to Sergey Korkin for providing the RT SORD code. The author thanks Jason Box, Carsten Brockmann, Luca Lelli and Thomas Wagner for the discussion of several topics related to this work.

Conflicts of Interest: The author declares no conflict of interest.

References

1. Liou, K.-N. *An Introduction to Atmospheric Radiation*; Academic Press: New York, NY, USA, 2002.
2. Cachorro, V.E.; Antuña-Sánchez, J.C.; de Frutos, A.M. SSolar-GOA v1.0: A simple, fast, and accurate Spectral solar radiative transfer for clear skies. *Geosci. Model Dev.* **2022**, *15*, 1689–1712. [[CrossRef](#)]
3. Mei, L.; Rozanov, V.; Burrows, J.P. A fast and accurate radiative transfer model for aerosol remote sensing. *J. Quant. Spectrosc. Radiat. Transf.* **2020**, *256*, 107270. [[CrossRef](#)]
4. Mei, L.; Rozanov, V.; Jiao, Z.; Burrows, J.P. A new snow bidirectional reflectance distribution function model in spectral regions from UV to SWIR: Model development and application to ground-based, aircraft and satellite observations. *ISPRS J. Photogramm. Remote Sens.* **2022**, *188*, 269–285. [[CrossRef](#)]
5. Kokhanovsky, A.A. *Snow Optics*; Springer Nature: Cham, Switzerland, 2021.
6. Kokhanovsky, A.A. Reflection of light from particulate media with irregularly shaped particles. *J. Quant. Spectrosc. Radiat. Transf.* **2005**, *96*, 1–10. [[CrossRef](#)]
7. Kokhanovsky, A.; Box, J.E.; Vandecrux, B.; Mankoff, K.D.; Lamare, M.; Smirnov, A.; Kern, M. The determination of snow albedo from satellite measurements using fast atmospheric correction technique. *Remote Sens.* **2020**, *12*, 234. [[CrossRef](#)]
8. Malinka, A.V.; Zege, E.P.; Katsev, I.L.; Istomina, L. Accounting for atmospheric effects in the interpretation of satellite and ground-based optical measurements. *J. Appl. Spectrosc.* **2016**, *83*, 741–749. [[CrossRef](#)]
9. Sobolev, V.V. *Light Scattering in Planetary Atmospheres*; Pergamon Press: Oxford, UK, 1975.
10. Katsev, I.L.; Prikhach, A.S.; Zege, E.P.; Grudo, J.O.; Kokhanovsky, A.A. Speeding up the aerosol optical thickness retrieval using analytical solutions of radiative transfer theory. *Atmos. Meas. Technol.* **2010**, *3*, 1403–1422. [[CrossRef](#)]
11. Katkovsky, L.V.; Martinov, A.O.; Siliuk, V.A.; Ivanov, D.A.; Kokhanovsky, A.A. Fast atmospheric correction method for hyperspectral data. *Remote Sens.* **2018**, *10*, 1698. [[CrossRef](#)]
12. Avaste, O.A.; Atroshenko, V.S. The accuracy of the Sobolev approximation. *Izv. Geophys.* **1960**, *3*, 45–49.
13. Busbridge, I.W.; Orchard, S.E. Reflection and transmission of light by a thick atmosphere according to a phase function $1+x\cos\theta$. *Astrophys. J.* **1967**, *149*, 655–664. [[CrossRef](#)]
14. Tomasi, C.; Petkov, B.H. Spectral calculations of Rayleigh-scattering optical depth at Arctic and Antarctic sites using a two-term algorithm. *J. Geophys. Res.* **2015**, *120*, 9514–9538. [[CrossRef](#)]
15. Six, D.; Fily, M.; Blarel, L.; Goloub, P. First aerosol optical thickness measurements at Dome C (east Antarctica), summer season 2003–2004. *Atmos. Env.* **2005**, *39*, 5041–5050. [[CrossRef](#)]
16. Ångström, A. On the atmospheric transmission of Sun radiation and on dust in the air. *Geogr. Ann.* **1929**, *11*, 156–166.
17. Iqbal, M. *An Introduction to Solar Radiation*; Elsevier: Amsterdam, The Netherlands, 1983.
18. Hansen, J.E.; Travis, L.D. Light scattering in planetary atmospheres. *Space Sci. Rev.* **1974**, *16*, 527–610. [[CrossRef](#)]
19. Tomasi, C.; Petkov, B.; Stone, R.S.; Benedetti, E.; Vitale, V.; Lupi, A.; Mazzola, M.; Lanconelli, C.; Herber, A.; von Hoyningen-Huene, W. Characterizing polar atmospheres and their effect on Rayleigh-scattering optical depth. *J. Geophys. Res.* **2010**, *115*, D02205. [[CrossRef](#)]
20. van de Hulst, H.C. *Multiple Light Scattering*; Academic Press: New York, NY, USA, 1980; Volume 1.
21. Coakley, J.; Chylek, P. The two-stream approximation in radiative transfer: Including the angle of the incident radiation. *J. Atmos. Sci.* **1975**, *32*, 409–418. [[CrossRef](#)]
22. Wiscombe, W.J.; Grams, G.W. The backscattered fraction in two-stream approximations. *J. Atmos. Sci.* **1976**, *33*, 2440–2451. [[CrossRef](#)]
23. Abramowitz, M.; Stegun, I. (Eds.) *Handbook of Mathematical Functions and Formulas, Graphs, and Mathematical Tables*. In *National Bureau of Standards Applied Mathematics Series*; U.S. Government Printing Office: Washington, DC, USA, 1964.
24. Kokhanovsky, A.A.; Mayer, B.; Rozanov, V.V. A parameterization of the diffuse transmittance and reflectance for aerosol remote sensing problems. *Atmos. Res.* **2005**, *73*, 37–43. [[CrossRef](#)]
25. Kokhanovsky, A.A.; Budak, V.P.; Cornet, C.; Duan, M.; Emde, C.; Katsev, I.L.; Klyukov, D.A.; Korkin, S.V.; C-Labonnote, L.; Mayer, B.; et al. Benchmark results in vector atmospheric radiative transfer. *J. Quant. Spectrosc. Radiat. Transf.* **2010**, *111*, 1931–1946. [[CrossRef](#)]
26. Korkin, S.; Lyapustin, A.; Sinyuk, A.; Holben, B.; Kokhanovsky, A. Vector radiative transfer code SORD: Performance analysis and quick start guide. *J. Quant. Spectrosc. Radiat. Transf.* **2017**, *200*, 295–310. [[CrossRef](#)]
27. Kokhanovsky, A.; Iodice, F.; Lelli, L.; Zschaegge, A.; De Quattro, N.; Gasbarra, D.; Retscher, C. Retrieval of total ozone column using high spatial resolution top-of-atmosphere measurements by OLCI/S-3 in the ozone Chappuis absorption band over bright underlying surfaces. *J. Quant. Spectrosc. Radiat. Transf.* **2021**, *276*, 107903. [[CrossRef](#)]

28. Green, A.E.; Wagner, J.C.; Mann, A. Analytic spectral functions for atmospheric transmittance calculations. *Appl. Opt.* **1988**, *27*, 2266–2272. [[CrossRef](#)]
29. Gorshelev, V.; Serdyuchenko, A.; Weber, M.; Chehade, W.; Burrows, J.P. High spectral resolution ozone absorption cross-sections—Part 1: Measurements, data analysis and comparison with previous measurements around 293 K. *Atmos. Meas. Technol.* **2014**, *7*, 609–624. [[CrossRef](#)]
30. Pierluissi, J.H.; Tsai, C.-M. Molecular transmission band model for oxygen in the visible. *Appl. Opt.* **1986**, *25*, 2458–2460. [[CrossRef](#)]
31. Zege, E.P.; Ivanov, A.P.; Katsev, I.L. *Image Transfer through Light Scattering Media*; Springer: Berlin, Germany, 1991.
32. Kokhanovsky, A.A.; Zege, E.P. Scattering optics of snow. *Appl. Opt.* **2004**, *43*, 1589–1602. [[CrossRef](#)]
33. Kokhanovsky, A.; Lamare, M.; Di Mauro, B.; Picard, G.; Arnaud, L.; Dumont, M.; Tuzet, F.; Brockmann, C.; Box, J.E. On the reflectance spectroscopy of snow. *Cryosphere* **2018**, *12*, 2371–2382. [[CrossRef](#)]
34. Kokhanovsky, A.; Lamare, M.; Danne, O.; Brockmann, C.; Dumont, M.; Picard, G.; Arnaud, L.; Favier, V.; Jourdain, B.; Meur, E.L.; et al. Retrieval of snow properties from the Sentinel-3 Ocean and Land Colour Instrument. *Remote Sens.* **2019**, *11*, 2280. [[CrossRef](#)]
35. Kokhanovsky, A.; Di Mauro, B.; Garzonio, R.; Colombo, R. Retrieval of dust properties from spectral snow reflectance measurements. *Front. Environ. Sci. Inform. Remote Sens.* **2021**, *9*, 644551. [[CrossRef](#)]
36. Picard, G.; Libois, Q.; Arnaud, L. Refinement of the ice absorption spectrum in the visible using radiance profile measurements in Antarctic snow. *Cryosphere* **2016**, *10*, 2655–2672. [[CrossRef](#)]
37. Warren, S.; Brand, R.E. Optical constants of ice from the ultraviolet to the microwave: A revised compilation. *J. Geophysical Research* **2008**, *113*, D14. [[CrossRef](#)]
38. Preusker, R.; Carbajal Henken, C.; Fischer, J. Retrieval of daytime total column water vapor from OLCI measurements over land surfaces. *Remote Sens.* **2021**, *13*, 932. [[CrossRef](#)]
39. Mazeran, C.; Rueskas, A. *Ocean Colour System Vicarious Calibration Tool Documentation*; EUMETSAT: Darmstadt, Germany, 2020.
40. Ricaud, P.; Gabard, B.; Derrien, S.; Chaboureaud, J.-P.; Rose, T.; Mombauer, A.; Czekala, H. HAMSTRAD-Tropo, A 183-GHz Radiometer Dedicated to Sound Tropospheric Water vapor Over Concordia Station, Antarctica. *IEEE Trans. Geosci. Remote Sens.* **2010**, *48*, 1365–1380. [[CrossRef](#)]
41. Kokhanovsky, A.A.; Di Mauro, B.; Colombo, R. Snow surface properties derived from PRISMA satellite data over the Nansen Ice Sheet (East Antarctica). *Front. Environ. Sci.* **2022**, *10*, 904585. [[CrossRef](#)]
42. Gay, M.; Fily, M.; Genthon, C.; Frezzotti, M.; Oerter, H.; Winther, J.-G. Snow grain-size measurements in Antarctica. *J. Glaciol.* **2002**, *48*, 527–535. [[CrossRef](#)]
43. Kokhanovsky, A.A. *Cloud Optics*; Springer: Berlin, Germany, 2006.
44. van de Hulst, H.C. *Light Scattering by Small Particles*; Dover: New York, NY, USA, 1981.